A Cavity-Enhanced UV Absorption Instrument for High Precision, Fast Time Response Ozone Measurements

Reem A. Hannun[1,2], Andrew K. Swanson[1,3], Steven A. Bailey[1], Thomas F. Hanisco[1], T. Paul Bui[4], Ilann Bourgeois[5,6], Jeff Peischl[5,6], Thomas B. Ryerson[5]

[1]Atmospheric Chemistry and Dynamics Laboratory, NASA Goddard Spaceflight Center, Greenbelt, MD, USA
[2]Joint Center for Earth Systems Technology, University of Maryland Baltimore County, Baltimore, MD, USA
[3]Universities Space Research Association, Columbia, MD, USA
[4]Earth Science Division, NASA Ames Research Center, Moffett Field, CA, USA
[5]NOAA Chemical Sciences Laboratory, Boulder, CO, USA
[6]Cooperative Institute for Research in Environmental Sciences, University of Colorado Boulder, Boulder, CO, USA

Correspondence to: Reem A. Hannun (reem.a.hannun@nasa.gov)

Abstract. The NASA Rapid Ozone Experiment (ROZE) is a broadband cavity-enhanced UV absorption instrument for the detection of *in situ* ozone (O_3). ROZE uses an incoherent LED light source coupled to a high-finesse optical cavity to achieve an effective pathlength of ~104 m. Due to its high-sensitivity and small optical cell volume, ROZE demonstrates a 1σ precision of 80 pptv (0.1 s) and 31 pptv (1 s), as well as an *e*-fold time response of 50 ms. ROZE can be operated in a range of field environments, including low- and high-altitude research aircraft, and is particularly suited to O_3 vertical flux measurements using the eddy covariance technique. ROZE was successfully integrated aboard the NASA DC-8 aircraft during July–September 2019 and validated against a well-established chemiluminescence measurement of O_3. A flight within the marine boundary layer also demonstrated flux measurement capabilities, and we observed a mean O_3 deposition velocity of 0.029 ± 0.005 cm s^{-1} to the ocean surface. The performance characteristics detailed below make ROZE a robust, versatile instrument for field measurements of O_3.

1   Introduction

In the troposphere, ozone (O_3) adversely affects air quality and acts as a greenhouse gas. Dry deposition to the Earth's terrestrial and oceanic surfaces represents a significant loss pathway for tropospheric O_3 (Young *et al.*, 2018) and thus influences tropospheric composition and O_3 pollution. Additionally, O_3 uptake through plant stomata leads to vegetation and crop damage (Ainsworth *et al.*, 2012; Mills *et al.*, 2018) and poor ecosystem health (Lombardozzi *et al.*, 2015), potentially amplifying the effects of O_3 on climate (Sitch *et al.*, 2007) and air quality (Sadiq *et al.*, 2017). Despite its role in the tropospheric O_3 budget, dry deposition velocities (v_d) of O_3 remain poorly constrained (Wesely and Hicks, 2000; Hardacre *et al.*, 2015). The observational records of terrestrial $v_d(O_3)$ are limited in number and do not capture the full variability in O_3 deposition rates with land cover (Clifton *et al.*, 2020a). Furthermore, studies of O_3 deposition to the ocean (e.g., Kawa and Pearson, 1989; Faloona *et al.*, 2005; Helmig *et al.*, 2012; Novak *et al.*, 2020) report deposition velocities of ~ 0.01–0.05 cm s^{-1}, which are 1–2 orders of magnitude lower than typical terrestrial values. Observations from Helmig *et al.* (2012) also suggest that O_3 deposition may vary with sea surface temperature. Global chemistry modeling frameworks that incorporate O_3 dry deposition (e.g., Bey *et al.*, 2001; Lamarque *et al.*, 2012) often apply fixed deposition rates to the ocean and heavily parameterized deposition schemes over land (Wesely, 1989). However, process-level representation of O_3 deposition improves agreement between modeled and observed surface O_3 concentrations (Clifton *et al.*, 2020b; Pound *et al.*, 2020). The range and variability in O_3 deposition rates thus motivates the need for further $v_d(O_3)$ measurements to refine both atmospheric and land surface model predictions.

Measurements of vertical O_3 fluxes are typically accomplished via eddy covariance (EC) analysis. The EC technique demands fast time-response, high-precision sensors to resolve the turbulence-driven variability in scalar concentrations. O_3 fluxes are therefore measured using highly sensitive O_3 detection methods such as chemiluminescence (e.g., Bariteau *et al.*, 2010; Muller *et al.*, 2010) and, more recently, chemical ionization mass spectrometry (CIMS) (Novak *et al.*, 2020). Chemiluminescence detectors employ either nitric oxide (NO) gas or organic dyes, which generate photons on reaction with O_3. While these instruments exhibit good sensitivity, they have practical drawbacks involving the use of cylinders containing toxic compressed gases or dangerous chemical dyes. Novak *et al.* (2020) successfully demonstrated the use of oxygen anion CIMS to measure O_3 and its vertical fluxes with a detection limit of < 0.005 cm s^{-1} over the ocean. To the best of our knowledge, ultraviolet (UV) absorption instruments have not previously been utilized for O_3 flux measurements due to insufficient sensitivity (e.g., Gao *et al.*, 2012). However, advancements in incoherent cavity-enhanced absorption spectroscopy (Fiedler *et al.*, 2003) facilitate the development of high-sensitivity sensors that are both robust and compact. Furthermore, UV absorption has the advantage of providing direct detection of O_3 without the need for a chemical titration source.

We report on the development of the NASA Rapid Ozone Experiment (ROZE), a cavity-enhanced UV absorption instrument for the *in-situ* detection of O_3. The long optical pathlength and small cavity volume enable high precision measurements in short averaging times, making ROZE suitable for O_3 flux measurements with the EC technique. The compact instrument design supports integration aboard research aircraft for both tropospheric and stratospheric deployment. We describe the principle of operation along with major instrument components and performance characteristics below. We also discuss the field performance of ROZE and demonstrate its EC capabilities using aircraft observations of O_3 deposition to the ocean surface.

2   Principle of operation

Incoherent broadband cavity-enhanced absorption spectroscopy (IBBCEAS) is an established tool for the detection of trace gas species (Fiedler *et al.*, 2003; Ball *et al.*, 2004; Washenfelder *et al.*, 2008) including O_3 (Darby *et al.*, 2012; Gomez and Rosen, 2013). IBBCEAS relies on a broadband, incoherent light source coupled to a high-finesse optical cavity. Typically, a multi-channel detector resolves structured absorption features in the ultraviolet (UV) or visible spectral regions. IBBCEAS exploits the long optical pathlength generated in the cavity to enhance sensitivity, comparable to other cavity-enhanced methods such as cavity ringdown spectroscopy (CRDS). However, unlike CRDS, IBBCEAS uses a relatively inexpensive light source as compared to a narrow linewidth laser. Furthermore, the incoherent light source relaxes the stringent requirements for cavity alignment that accompany other cavity enhanced methods such as CRDS, enabling a more robust instrument configuration for field environments.

ROZE employs the IBBCEAS technique for high-sensitivity measurements of O_3. As illustrated in Figure 1, a light-emitting diode (LED) in the UV ($\lambda_{max} = 265$ nm) is collimated with an aspheric lens and coupled into an optical cavity formed by two high-reflectivity mirrors. Exiting light is passed to a photomultiplier tube (PMT) detector through a series of collection and filter optics. Figure 2 depicts the normalized detected LED intensity, which accounts for the LED spectral irradiance, the optical bandpass filter transmission, and the wavelength dependent PMT response. The LED spectrum overlaps with the O_3 Hartley band, and any O_3 present in the sample cell attenuates the light intensity received at the detector. The use of optical filters on the PMT precludes the need for wavelength resolution from a grating spectrometer and simplifies data reduction. Section 3.1 provides further details on the ROZE optical system.

Attenuation of light intensity in an IBBCEAS cavity results from trace gas absorption as well as extinction due to the mirrors and Rayleigh scatter. Accounting for these additional losses, the Beer-Lambert absorption coefficient, α_{abs}, is related to the observed change in intensity transmitted through the cavity as follows (Washenfelder *et al.*, 2008):

$$\alpha_{abs} = \left(\frac{I_0 - I}{I}\right)\left(\frac{1-R}{d} + \alpha_{Ray}\right) \tag{1}$$

Here, I_0 is light intensity in the absence of any absorbing species, I is the intensity attenuated due to absorption, R is the mirror reflectivity, d is the physical distance separating the cavity mirrors, and α_{Ray} is the extinction due to Rayleigh scatter, a non-negligible component in the UV. The term $(1-R)/d$ gives the theoretical cavity loss, α_{cav}, and represents the inverse of the maximum effective pathlength, L_{eff}. In cavity-enhanced techniques, L_{eff} can be many orders of magnitude larger than d, resulting in high sensitivity to the absorbing species. Equation 1 can also be expressed as $\alpha_{abs} = N\sigma_{abs}$, where N is number density of the absorbing species and σ_{abs} is the absorption cross section. In principle, accurate trace gas measurements require calibration of the α_{cav} term yielding L_{eff}, knowledge of the Rayleigh and absorption cross sections in the detected spectral region, and the measured I_0 and I terms. The data processing and calibration for ROZE will be discussed in Sections 3.4 and 4.1, respectively.

3   Instrument description

ROZE consists of three main subsystems housed in a compact 58 cm long x 44 cm wide x 18 cm high chassis, with a total instrument weight of 19 kg (Figure 3). The optical plate – a custom aluminum honeycomb panel supported by friction dampened spring vibration isolators – provides a stable platform for the optical components, consisting of the LED, sample cell, and PMT. The remaining subsystems include the flow handling and the data acquisition. Each major subsystem is described in greater detail below. ROZE operates at 24 V_{DC} with a low-profile AC-DC switching power supply (Vicor VI-LU3-IU) capable of running off 115 or 230 V_{AC} (47–440 Hz), which can be supplied directly from the aircraft. Power consumption is less than 200 W and typically ~100 W. Table 1 summarizes ROZE design and performance characteristics.

3.1   Optical components

3.1.1   LED assembly

A UV LED (λ_{max} = 265 nm, FWHM = 10 nm) (Thorlabs M265D2) is mounted to a custom heat sink and temperature controlled to 30 °C with a thermo-electric cooler (TE Technology CH-21-1.0-1.3; Wavelength Electronics PTC2.5K-CH). The LED output power is separately monitored by a photodiode (Marktech MTPD4400D-1.5) inserted into the edge of a lens tube that holds the LED. The LED assembly attaches to a custom cage mount system that also houses the associated optics, including the aspheric collimation lens (f = 79 mm, Thorlabs ASL10142M) and a beam expander (Thorlabs BE02-UVB) in reverse to shrink the collimated LED output. For compactness, the LED assembly and cage system are mounted parallel to the sample cell, and two mirrors (Thorlabs NB1-K04) turn the beam 180° into the cell (see Figure 3).

3.1.2   Sample cell

The sample cell is manufactured from an aluminum alloy tube measuring 30 cm in length with a 1.2 cm inner diameter. The cell mirrors (Layertech 109561) have a reflectivity of R > 99.7% over the detected spectral range (Figure 2) and a 500 mm radius of curvature. The mirrors are held directly at the cell ends on face type o-ring seals using custom, non-adjustable mounts fastened to tube collars. The mirror positions are configured to maximize centricity. Two gas ports direct the sample flow into and out of the cell at right angles. The sample enters through a custom stainless steel cylindrical diffuser, a ring with circumferential openings

adjacent to the cell mirrors, that nests within the cell tube orthogonal to the ports. The diffuser helps minimize noise due to Rayleigh scatter from turbulence within the cell at high sample flow rates. A 2-micron pleated mesh filter (Swagelock) affixes to the sample cell inlet port to exclude dust and other particles from affecting the mirror reflectivity, as the mirrors are not independently purged. A pressure transducer (Omega MMA015V10P4K1T4A6) measures the cell pressure from a port near the cell center. The entire cell is thermally regulated to 35 °C using resistive heaters and a precision heater control (Wavelength Electronic PTC2.5K-CH).

3.1.3 PMT assembly

A PMT (Hamamatsu H10720-113) operating in analog mode collects the light exiting the cell. Two optical bandpass filters (Thorlabs FGUV5-UV, Semrock FF01-260/16) transmit the cell output to a collection lens (f = 35 mm, Thorlabs LA4052-UV), which images the beam onto the PMT photocathode. A UV window (Thorlabs WG40530-UV) glued into a custom PEEK lens tube adapter seals to the PMT face with a Viton gasket, creating a leak-tight package for low-pressure (high-altitude) operation. The PMT is thermally stabilized to 35 °C in the same manner as the sample cell. The PMT signal is passed to an amplifier circuit (Analog Devices EVAL-ADA4625-1ARDZ) before digitization by the data acquisition system described below.

3.2 Flow system

The ROZE flow system is designed to achieve rapid flushing of the detection cell as required for fast concentration measurements. However, ROZE samples at ambient pressure to maximize sensitivity, necessitating high throughput with a minimal pressure differential. ROZE utilizes a linear diaphragm pump (Thomas 6025SE-150113) that can achieve a flow rate of up to 18 standard liter per minute (SLM) through the system. The pump speed can also be adjusted by varying the supply current and has three pre-set speeds (e.g., 2, 5, 11 SLM) that can be changed by a switch on the chassis front panel. A flow meter (Honeywell AWM5104) located between the cell exhaust and the pump monitors the sample flow in real time. ROZE uses fluorinated ethylene propylene (FEP) tubing both external and internal to the chassis upstream of the sample cell. External to the chassis, the inlet details depend on the aircraft platform. ROZE has previously used the inlet detailed in Cazorla *et al.* (2015) when flying on the NASA DC-8 aircraft. The instrument exhaust plumbs directly to an exhaust port near the rear of the aircraft.

ROZE O_3 measurements also require knowledge of the reference intensity (I_0) as detailed in Equation 1. A 3-way solenoid valve (NResearch TC648T032) switches between the sample line (ambient air from the aircraft inlet) and the zero port, which attaches to an internal Carulite O_3 scrubber (2B Technologies) to produce O_3-free air. Periodic zeroing during operation captures long-term drift in I_0 due to the LED output, PMT response, and changing environmental conditions. Typically, the instrument opens to the O_3 scrubber for 10 seconds every 5 minutes.

3.3 Data acquisition

ROZE utilizes a CompactRIO (National Instruments cRIO-9030) that incorporates a real-time operating system and a Field Programmable Gate Array (FPGA). The FPGA is configured for modulation of the LED and subsequent digitization of the PMT signal. To improve measurement precision and remove background due to ambient light scatter, the FPGA modulates the LED at 1 kHz with a 90% duty cycle (900 µs ON/100 µs OFF) via an external LED driver (Wavelength Electronics FL591FL). A 16-bit Analog to Digital Converter (ADC) digitizes the amplified PMT signal at a digitization rate of 100 kHz. This high rate enables us to average each LED ON and OFF pulse amplitude. We then take the difference of the ON and OFF signals to remove background noise, both optical (i.e., stray light) and electronic. The 1 kHz differences are further averaged to 10 Hz and recorded. Other

diagnostic housekeeping variables (e.g., sample flow, temperatures, LED power) are recorded at 1 Hz. Additionally, an analog output commands the 3-way valve to open to the zero line with a user-defined period and duration.

3.4 Data processing

In practice, the absorbance calculation for ROZE factors in the pressure difference between the sample and zero lines, as derived by Min *et al.* (2016):

$$\alpha_{O3} = \left(\frac{I_Z}{I} - 1\right)\left(\alpha_{cav} + \alpha_{Ray,Z}\right) + \Delta\alpha_{Ray} \tag{2}$$

Analogous to Equation 1, I_Z is the intensity measured when sampling through the zero line (O_3-scrubbed air), I is the intensity when sampling ambient air, and $\Delta\alpha_{Ray} = \alpha_{Ray,Z} - \alpha_{Ray,S}$, where $\alpha_{Ray,Z}$ and $\alpha_{Ray,S}$ give the Rayleigh extinction ($\alpha_{Ray} = N_{air}\sigma_{Ray}$) of the zero and the sample respectively. Using the measured I_Z, I, and the known Rayleigh scatter and O_3 absorption cross sections, the O_3 number density can then be determined as $\alpha_{O3} = N_{O3}\sigma_{O3}$. The Rayleigh scattering (Bucholtz, 1995) and O_3 absorption (Serdyuchenko *et al.*, 2014) cross sections are calculated as the weighted average over the collected spectral range (Figure 2). Using known cross sections and a calibrated α_{cav} (inverse effective pathlength), the observed change in intensity yields a direct measure of the O_3 concentration.

4 Performance

4.1 Sensitivity and calibration

The effective pathlength of the ROZE optical cavity determines the instrument sensitivity to O_3 (i.e., the attenuation in intensity per unit O_3). The cavity extinction, and thus the effective pathlength, are dictated by the mirror reflectivity as described above but require independent calibration. Calibration can be accomplished via standard addition of O_3 or Rayleigh attenuation (in the absence of absorbing species) at varied sample pressures. The former method relies on commercially available O_3 generators or sensors for verification, which lack the required accuracy and may drift over time. In contrast, the Rayleigh calibration provides a convenient and straightforward alternative. Both methods are described below.

Figure 4a depicts the ROZE calibration using known concentrations of O_3. A commercial O_3 source (2B Technologies 306) generated known amounts of O_3, with the zero O_3 addition serving as the I_Z baseline. Per Equation 2, the slope of the observed attenuation ($dI = I_Z/I - 1$) as a function of O_3 number density is proportional to the remaining extinction terms ($\alpha_{cav} + \alpha_{Ray}$). Solving for α_{cav} using the O_3 cross section and the calculated Rayleigh extinction, the calibration yields an effective pathlength of $L_{\text{eff}} = 108 \pm 6$ m. The alternate calibration uses the Rayleigh extinction in zero air over a range of cell pressures (Figure 4b). In the absence of absorbing species, an expression for α_{cav} can be derived following the approach in Washenfelder *et al.* (2008) as:

$$\alpha_{Ray} = \left(\frac{I_0}{I} - 1\right)\alpha_{cav} \tag{3}$$

I_0 represents the intensity at vacuum, which can be extrapolated from a linear fit of counts as a function of cell pressure. The slope of the observed change in intensity with number density therefore yields a direct measure of the cavity extinction, resulting in an effective pathlength of 104 ± 4 m. The two methods agree to within the 2σ fit uncertainties, and we use L_{eff} as determined by the Rayleigh calibration for subsequent calculations.

4.2 Precision and accuracy

The major contributions to instrument noise include PMT electrical noise and differential scatter or absorption due to non-uniform flow within the sample cell at high flow rates. The flow diffuser (see Section 3.1.2) effectively reduces the flow noise, while decreasing the gain on the PMT amplifier circuit minimizes the PMT electrical noise. The ROZE precision can be determined from the continuous sampling of zero air at a constant pressure. Figure 5 depicts the Allan-Welre deviation plot (1σ) for ROZE (in pptv O_3 equivalents) as calculated from optical extinction measurements of zero air acquired over 1.5 hours at 944 mbar. For short integration times (< 10 s), a fit of the data gives a $\tau^{-0.47}$ decay, indicating the Allan deviation closely follows the square root of the averaging time ($\tau^{-1/2}$) as expected for white noise. At the native 0.1 s sampling rate, the 1σ precision for O_3 is 80 pptv and reduces to 31 pptv with 1 s averaging. For the given cell pressure and a temperature of 35 °C, this translates to a 1σ precision of 6.7 x 10^8 molecules cm^{-3} (1 s average) of O_3.

The absolute accuracy of the ROZE measurement depends on uncertainties in the literature-reported values of the O_3 and Rayleigh cross sections, the measured cell temperature and pressure, and the calibrated cavity extinction. The reported O_3 absorption cross section has an uncertainty of 2% (Gorshelev *et al.*, 2014), and we estimate a conservative uncertainty of 3% for the Rayleigh scattering cross section (Bucholtz, 1995). The cell pressure and temperature are accurate to within 0.2% and 0.5% respectively, and the calibrated cavity extinction has an additional 4% slope uncertainty from the linear fit. These errors propagate through Equation 2 to yield a total measurement uncertainty of 6.2% in the O_3 number density.

4.3 Response time

The flush time of the sample cell limits the true instrument response time despite the 10 Hz data acquisition rate. A rapid flush rate is critical for high spatial resolution measurements from a fast-moving platform. Additionally, fast concentration measurements are required for sampling of turbulent eddies for airborne EC, and the necessary time response scales with aircraft speed. Response times of 10 Hz are typically considered sufficient for ground-based EC (Aubinet *et al.*, 2012), while for airborne EC, a response time of 1–5 Hz are typically sufficient due to larger eddy scales at altitude (Wolfe *et al.*, 2018). Figure 6a shows the instantaneous instrument response to a series of 10 ms pulses of O_3 injected into a zero-air carrier flow using a fast switching valve (The Lee Company, IEP series). During this experiment, the pump maintained a sample flow rate of 18 SLM. A series of exponential decay fits for several O_3 pulses yields an *e*-folding time constant of $\tau_r = 50 \pm 4$ ms (Figure 6b), which corresponds to a 3*e*-fold cell flush rate of 9.5 Hz.

5 Field demonstration

ROZE can be operated on both low- and high-altitude aircraft platforms. Though ROZE has not yet flown on a high-altitude unpressurized aircraft (such as the NASA ER-2), laboratory experiments in a thermal vacuum chamber have demonstrated no loss of performance down to a pressure and temperature of 50 mbar and 250 K (results not shown). In summer 2019, ROZE flew aboard the NASA DC-8 for the Fire Influence on Regional to Global Environments Experiment, Air Quality (FIREX-AQ) campaign over the Central and Northwest United States. The instrument operated as described above, with the addition of an inline particle filter (Balston 9922-05-DQ) to protect the cavity mirrors from fine particulates in the targeted smoke plumes. Although more aggressive filtering comes at the cost of reduced flow rates and thus lowers the instrument response time, O_3 deposition measurements were not a primary objective of FIREX-AQ. Below, we detail comparisons of ROZE against an established O_3 measurement.

Additionally, level flight legs in the marine boundary layer during a flight over the ocean provide an initial demonstration of O_3 vertical flux measurements.

5.1 FIREX-AQ validation against chemiluminescence

FIREX-AQ flights targeted forest wildfires and agricultural burns. In fresh, concentrated smoke plumes, UV-active species such as SO_2, aromatic hydrocarbons, and other volatile organic compounds (VOC) can give rise to positive artifacts in the O_3 signal (Long *et al.*, 2020), as the UV absorption technique lacks selectivity (see Birks, 2015). The potential for overestimating O_3 due to interfering absorbers can also be of concern in highly polluted urban environments (e.g., Spicer *et al.*, 2010). In general, these studies demonstrate that UV absorption based O_3 analyzers are not always ideally suited to such applications. Nonetheless, modifications such using an O_3 selective scrubber material (e.g., heated graphite) to preserve VOC and thus account for interferences in the background (I_z) signal have been shown to reduce positive artifacts (Turnipseed *et al.*, 2017). As we did not substitute the ROZE scrubber for the FIREX-AQ deployment, an on-board, independent measurement of formaldehyde (HCHO) was used as a plume indicator. ROZE O_3 data are therefore quality filtered to remove points sampled within dense smoke plumes using HCHO mixing ratios above 5 ppbv.

The DC-8 FIREX-AQ payload included the NOAA Nitrogen Oxides and Ozone (NOyO3) instrument, a well-established O_3 measurement using the chemiluminescence technique (Ryerson *et al.*, 2000; Bourgeois *et al.*, 2020). ROZE operated simultaneously with the NOyO3 instrument during several flights. Figure 7 shows a comparison of ROZE and NOyO3 data for the July 30, 2019 flight over the Northwestern United States. During this flight, no fresh smoke plumes were sampled, and no filtering of the ROZE data was necessary. Figure 7a depicts a ~25 min subset of the full timeseries to illustrate the ROZE instrument precision. Both measurements (averaged to 1 s) track the dynamic features in O_3 mixing ratios well. The correlation plot for the full flight (Figure 7b) demonstrates strong agreement between the two measurements, with a slope of 0.98 ± 0.01 and an intercept of 0.17 ± 0.02 ppbv O_3 ($r^2 = 0.99$). Note the intercept is less than 1% of the minimum observed O_3 mixing ratios for this flight. Comparisons for 15 flights from the campaign indicate a range of 0.96–1.04 in slope and -1.6–1.4 ppbv O_3 in intercept (in all cases, this offset is < 4% of the minimum measured O_3), consistent with the measurement uncertainty.

5.2 Ozone flux measurements

5.2.1 Eddy covariance flux

The vertical flux of O_3 can be directly quantified using the eddy covariance (EC) technique. EC defines the flux (F) as the time or spatially averaged covariances in the vertical wind speed (w) and the scalar species of interest (in this case the O_3 mixing ratio X_{O3}):

$$F_{O3} = \langle w' X_{O3}' \rangle \qquad (4)$$

In the equation above, the primes denote instantaneous deviations from the mean value, and the brackets indicate an average over a prescribed interval as discussed below. Since deposition dominates transfer across the air-surface interface, the O_3 flux can instead be expressed as a transfer rate or deposition velocity (v_d):

$$v_d = -\frac{F_{O3}}{\bar{X}_{O3}} \qquad (5)$$

Here, the overbar indicates the mean O_3 mixing ratio over the averaging period. The deposition velocity, in units of cm s^{-1}, yields a normalized metric of the deposition efficiency and incorporates both chemical and physical transfer processes.

During the FIREX-AQ campaign, the flight on July 17, 2019 contained a level segment within the turbulent marine boundary layer suitable for EC. The flux transects were located over the Pacific Ocean, ~200 miles southwest of the Los Angeles Basin. To quantify O_3 deposition, the Meteorological Measurement System (MMS) instrument provided 3-D wind vector data (Chan *et al.*, 1998), which were used in conjunction with ROZE O_3 measurements. A 1-D coordinate rotation was applied to the wind vector to force the mean vertical wind to zero, and the native 20 Hz MMS data was averaged to the ROZE 10 Hz time base. Note that the additional particle filter reduced the ROZE sample flow to 11.3 SLM, and we estimate the time constant from the decay in intensity following the zero-O_3 additions as τ_r = 90 ms (5.5 Hz 3e-fold flush rate). We also use 20 Hz water vapor measurements from the open path Diode Laser Hygrometer (DLH) (Diskin *et al.*, 2002) as a benchmark for the flux performance. 20 Hz DLH data were averaged to the ROZE time base and used to apply a moist-to-dry air correction for raw O_3 observations, negating the need for density corrections to the calculated flux (Webb *et al.*, 1980). This density correction reduces the O_3 flux by ~6%. For the EC calculations, we selected two ~50 km transects with consistent aircraft heading, stationary flow, and level altitude (~170 m). Scalar data were detrended by subtracting a 20 second running mean, which corresponds to spatial scales of ~2.7 km. The detrending length was chosen to remove non-turbulent variability (e.g., changing chemical conditions) while still capturing the largest flux-contributing eddies as identified by examination of the co-spectra from a range of averaging windows. Scalar data were then synchronized to the vertical winds using a time-lag that optimized covariance.

5.2.2 Spectral analysis

Spectral analysis aids in decomposing the contributions of eddies at different scales (frequencies) to the overall signal and provides a quality assessment of the ROZE flux measurements. Figure 8 displays the lag-covariance, power spectrum, and co-spectrum for O_3 and vertical wind fluctuations generated using fast Fourier transforms (FFTs) for a single transect. The spectra for water vapor are also displayed for comparison. The lagged cross-cross covariance functions (Figure 8a) demonstrate defined peaks at lags of < 0.5 s, with the peak non-normalized covariance yielding a measure of the flux. Dividing out the background O_3 mixing ratio of 29 ppbv, we find a mean deposition velocity of 0.029 cm s^{-1} for the two transects. The power spectra in Figure 8b show that vertical winds follow the theoretical $f^{-5/3}$ decay expected in the inertial subrange (Kaimal *et al.*, 1972). The slope for the O_3 power spectrum initially follows the same decay but flattens at ~1 Hz, indicating that the turbulence-driven variability in O_3 approaches the ROZE precision limit in higher-frequency eddies. However, the normalized frequency-weighted co-spectral power of w' with X_{O3}' (Figure 8c, solid lines) shows that flux carrying eddies below ~0.6 Hz dominate the total signal. The ogive, the cumulative integral of the co-spectrum (Fig. 8c, dashed lines) further indicates that 99% of flux carrying eddies occur at frequencies below ~4 Hz. These results demonstrate the adequate ROZE time response for airborne EC.

5.2.3 Flux measurement uncertainty

Detailed methods to quantify flux errors for airborne EC can be found elsewhere (Lenschow *et al.*, 1994; Langford *et al.*, 2015; Wolfe *et al.*, 2018). Here, we aim to quantify the random and systematic flux errors that reflect the overall instrument performance. We use the empirical formulation of Finkelstein and Sims (2001) to estimate the total random error (RE$_{TOT}$) as the variance of the scalar-wind covariance. In this approach, the RE$_{TOT}$ is determined using auto- and cross-correlation functions (as in Figure 8a) over lag times that are sufficient to capture the timescale of the correlation (here ~10 s). Averaging over the flux legs yields a RE$_{TOT}$ of 0.005 cm s^{-1}. RE$_{TOT}$ encompasses both instrument noise as well as error from the random sampling of turbulence. To isolate the RE component due solely to instrument noise (RE$_{noise}$), we follow the approach of Mauder *et al.* (2013). In this method, the standard deviation of the instrument noise is derived from the scalar auto-covariance and then propagated to determine its contribution to the to the cross-covariance uncertainty. Note that RE$_{noise}$ still depends on the turbulence regime and therefore varies

with atmospheric conditions. We calculate RE_{noise} to be 0.0015 cm s^{-1} averaging over the two flux transects. These results indicate that instrument noise constitutes ~30% of the total random error.

Additionally, the instrument time response can lead to systematic flux errors as a consequence of undersampling contributions from high-frequency eddies. We determine the systematic error due to the instrument response time (SE_{RT}) following the Horst (1997) model, whereby the attenuation in the measured signal can be expressed as a co-spectral transfer function based on the characteristic instrument response time. Using the ROZE response time of τ_r = 90 ms, we determine SE_{RT} as < 2%, indicating minimal attenuation in the measured flux signal.

6   Summary and conclusions

The NASA ROZE instrument provides high sensitivity, fast time response measurements of O_3 via broadband cavity-enhanced UV absorption. The compact, robust instrument package is adaptable to diverse field environments, including low- and high-altitude aircraft platforms. ROZE currently achieves a 1σ precision of ~30 pptv s^{-1} and an overall accuracy of 6.2%. ROZE was successfully integrated aboard the NASA DC-8 aircraft, and the field performance compares favorably with an independent O_3 measurement to within ROZE uncertainty. The maximum observed time response for laboratory tests was 50 ms, with additional filtering during aircraft operation slowing the time response to 90 ms. The instrument precision and time response make ROZE particularly well suited for vertical O_3 flux measurements using eddy covariance analysis. ROZE has measured O_3 deposition velocities of 0.029 ± 0.005 cm s^{-1} to the ocean surface, with minimal (< 2%) response-time attenuation in the flux signal. The demonstrated performance of ROZE makes the instrument an ideal and versatile option for field measurements of both O_3 concentrations and fluxes.

Data availability

The FIREX-AQ data for O_3 (ROZE and NOyO3), water vapor (DLH), formaldehyde (ISAF), and 3-D winds (MMS) are publicly available at https://www-air.larc.nasa.gov/missions/firex-aq/.

Acknowledgements

This work was supported by the NASA Internal Research and Development (IRAD) program, the NASA Upper Atmosphere Research Program, and the NASA Tropospheric Chemistry Program. The aircraft flight opportunity was provided by the NASA/NOAA FIREX-AQ project and the NASA Student Airborne Research Program (SARP). We would like to acknowledge the DLH instrument team (Glenn Diskin, et al.) for the water vapor measurements used in the eddy covariance analysis. We would additionally like to thank Jason St. Clair and Glenn Wolfe for helpful comments on the manuscript and Glenn Wolfe for his help with the eddy covariance analysis.

References

Ainsworth, E. A. *et al.* (2012) 'The Effects of Tropospheric Ozone on Net Primary Productivity and Implications for Climate Change', *Annual Review of Plant Biology*, 63(1), pp. 637–661. doi: 10.1146/annurev-arplant-042110-103829.

Aubinet, M., Vesala, T. and Papale, D. (eds) (2012) *Eddy Covariance, Eddy Covariance: A Practical Guide to Measurement and Data Analysis*. Dordrecht: Springer Netherlands. doi: 10.1007/978-94-007-2351-1.

325 Ball, S. M., Langridge, J. M. and Jones, R. L. (2004) 'Broadband cavity enhanced absorption spectroscopy using light emitting diodes', *Chemical Physics Letters*, 398(1–3), pp. 68–74. doi: 10.1016/j.cplett.2004.08.144.

Bariteau, L. *et al.* (2010) 'Determination of oceanic ozone deposition by ship-borne eddy covariance flux measurements', *Atmospheric Measurement Techniques*, 3(2), pp. 441–455. doi: 10.5194/amt-3-441-2010.

Bey, I. *et al.* (2001) 'Global modeling of tropospheric chemistry with assimilated meteorology: Model description and evaluation',
330 *Journal of Geophysical Research: Atmospheres*, 106(D19), pp. 23073–23095. doi: 10.1029/2001JD000807.

Birks, J. (2015) *UV-Abosorbing Interferences in Ozone Monitors*. Available at: https://twobtech.com/docs/tech_notes/TN040.pdf.

Bourgeois, I. *et al.* (2020) 'Global-scale distribution of ozone in the remote troposphere from the ATom and HIPPO airborne field missions', *Atmospheric Chemistry and Physics*, 20(17), pp. 10611–10635. doi: 10.5194/acp-20-10611-2020.

Bucholtz, A. (1995) 'Rayleigh-scattering calculations for the terrestrial atmosphere', *Applied Optics*, 34(15), p. 2765. doi:
335 10.1364/AO.34.002765.

Cazorla, M. *et al.* (2015) 'A new airborne laser-induced fluorescence instrument for in situ detection of formaldehyde throughout the troposphere and lower stratosphere', *Atmospheric Measurement Techniques*, 8(2), pp. 541–552. doi: 10.5194/amt-8-541-2015.

Chan, K. R. *et al.* (1998) 'Turbulence measurements by the DC-8 Meteorological Measurement System', *Geophysical Research Letters*, 25(9), pp. 1355–1358. doi: 10.1029/97GL03590.

340 Clifton, Olivia E. *et al.* (2020) 'Dry Deposition of Ozone Over Land: Processes, Measurement, and Modeling', *Reviews of Geophysics*, 58(1). doi: 10.1029/2019RG000670.

Clifton, O. E. *et al.* (2020) 'Influence of Dynamic Ozone Dry Deposition on Ozone Pollution', *Journal of Geophysical Research: Atmospheres*, p. e2020JD032398. doi: 10.1029/2020jd032398.

Darby, S. B., Smith, P. D. and Venables, D. S. (2012) 'Cavity-enhanced absorption using an atomic line source: application to
345 deep-UV measurements', *The Analyst*, 137(10), p. 2318. doi: 10.1039/c2an35149h.

Diskin, G. S. *et al.* (2002) 'Open-path airborne tunable diode laser hygrometer', in Fried, A. (ed.) *Proc SPIE, Diode Lasers and Applications in Atmospheric Sensing*, p. 196. doi: 10.1117/12.453736.

Faloona, I. *et al.* (2005) 'Observations of Entrainment in Eastern Pacific Marine Stratocumulus Using Three Conserved Scalars', *Journal of the Atmospheric Sciences*, 62(9), pp. 3268–3285. doi: 10.1175/JAS3541.1.

350 Fiedler, S. E., Hese, A. and Ruth, A. A. (2003) 'Incoherent broad-band cavity-enhanced absorption spectroscopy', *Chemical Physics Letters*, 371(3–4), pp. 284–294. doi: 10.1016/S0009-2614(03)00263-X.

Finkelstein, P. L. and Sims, P. F. (2001) 'Sampling error in eddy correlation flux measurements', *Journal of Geophysical Research: Atmospheres*, 106(D4), pp. 3503–3509. doi: 10.1029/2000JD900731.

Gao, R. S. *et al.* (2012) 'A compact, fast UV photometer for measurement of ozone from research aircraft', *Atmospheric*
355 *Measurement Techniques*, 5(9), pp. 2201–2210. doi: 10.5194/amt-5-2201-2012.

Gomez, A. L. and Rosen, E. P. (2013) 'Fast response cavity enhanced ozone monitor', *Atmospheric Measurement Techniques*, 6(2), pp. 487–494. doi: 10.5194/amt-6-487-2013.

Gorshelev, V. *et al.* (2014) 'High spectral resolution ozone absorption cross-sections – Part 1: Measurements, data analysis and comparison with previous measurements around 293 K', *Atmospheric Measurement Techniques*, 7(2), pp. 609–624.
360 doi: 10.5194/amt-7-609-2014.

Hardacre, C., Wild, O. and Emberson, L. (2015) 'An evaluation of ozone dry deposition in global scale chemistry climate models', *Atmospheric Chemistry and Physics*, 15(11), pp. 6419–6436. doi: 10.5194/acp-15-6419-2015.

Helmig, D. *et al.* (2012) 'Atmosphere-ocean ozone fluxes during the TexAQS 2006, STRATUS 2006, GOMECC 2007, GasEx 2008, and AMMA 2008 cruises', *Journal of Geophysical Research: Atmospheres*, 117(D4). doi: 10.1029/2011JD015955.

365 Horst, T. W. (1997) 'A simple formula for the attenuation of eddy fluxes measured with first-order-response scalar sensors', *Boundary-Layer Meteorology*, 82(2), pp. 219–233. doi: 10.1023/A:1000229130034.

Kaimal, J. C. *et al.* (1972) 'Spectral characteristics of surface-layer turbulence', *Quarterly Journal of the Royal Meteorological Society*, 98(417), pp. 563–589. doi: 10.1002/qj.49709841707.

Kawa, S. R. and Pearson, R. (1989) 'Ozone budgets from the dynamics and chemistry of marine stratocumulus experiment',
370 *Journal of Geophysical Research*, 94(D7), p. 9809. doi: 10.1029/JD094iD07p09809.

Lamarque, J.-F. *et al.* (2012) 'CAM-chem: description and evaluation of interactive atmospheric chemistry in the Community Earth System Model', *Geoscientific Model Development*, 5(2), pp. 369–411. doi: 10.5194/gmd-5-369-2012.

Langford, B. *et al.* (2015) 'Eddy-covariance data with low signal-to-noise ratio: time-lag determination, uncertainties and limit of detection', *Atmospheric Measurement Techniques*, 8(10), pp. 4197–4213. doi: 10.5194/amt-8-4197-2015.

375 Lenschow, D. H., Mann, J. and Kristensen, L. (1994) 'How Long Is Long Enough When Measuring Fluxes and Other Turbulence Statistics?', *Journal of Atmospheric and Oceanic Technology*, 11(3), pp. 661–673. doi: 10.1175/1520-0426(1994)011<0661:HLILEW>2.0.CO;2.

Lombardozzi, D. *et al.* (2015) 'The influence of chronic ozone exposure on global carbon and water cycles', *Journal of Climate*, 28(1), pp. 292–305. doi: 10.1175/JCLI-D-14-00223.1.

380 Long, R. W. *et al.* (2020) 'Comparison of Ozone Measurement Methods in Biomass Burning Smoke: An evaluation under field and laboratory conditions', *Atmospheric Measurement Techniques Discussions*, 2020, pp. 1–33. doi: 10.5194/amt-2020-383.

Mauder, M. *et al.* (2013) 'A strategy for quality and uncertainty assessment of long-term eddy-covariance measurements', *Agricultural and Forest Meteorology*, 169, pp. 122–135. doi: 10.1016/j.agrformet.2012.09.006.

Mills, G. *et al.* (2018) 'Ozone pollution will compromise efforts to increase global wheat production', *Global Change Biology*, 385 24(8), pp. 3560–3574. doi: 10.1111/gcb.14157.

Min, K.-E. *et al.* (2016) 'A broadband cavity enhanced absorption spectrometer for aircraft measurements of glyoxal, methylglyoxal, nitrous acid, nitrogen dioxide, and water vapor', *Atmospheric Measurement Techniques*, 9(2), pp. 423–440. doi: 10.5194/amt-9-423-2016.

Muller, J. B. A. *et al.* (2010) 'Sources of uncertainty in eddy covariance ozone flux measurements made by dry chemiluminescence 390 fast response analysers', *Atmospheric Measurement Techniques*, 3(1), pp. 163–176. doi: 10.5194/amt-3-163-2010.

Novak, G. A., Vermeuel, M. P. and Bertram, T. H. (2020) 'Simultaneous detection of ozone and nitrogen dioxide by oxygen anion chemical ionization mass spectrometry: a fast-time-response sensor suitable for eddy covariance measurements', *Atmospheric Measurement Techniques*, 13(4), pp. 1887–1907. doi: 10.5194/amt-13-1887-2020.

Pound, R. J. *et al.* (2020) 'Influences of oceanic ozone deposition on tropospheric photochemistry', *Atmospheric Chemistry and* 395 *Physics*, 20(7), pp. 4227–4239. doi: 10.5194/acp-20-4227-2020.

Ryerson, T. B., Williams, E. J. and Fehsenfeld, F. C. (2000) 'An efficient photolysis system for fast-response NO2 measurements', *Journal of Geophysical Research: Atmospheres*, 105(D21), pp. 26447–26461. doi: 10.1029/2000JD900389.

Sadiq, M. *et al.* (2017) 'Effects of ozone–vegetation coupling on surface ozone air quality via biogeochemical and meteorological feedbacks', *Atmospheric Chemistry and Physics*, 17(4), pp. 3055–3066. doi: 10.5194/acp-17-3055-2017.

400 Serdyuchenko, A. *et al.* (2014) 'High spectral resolution ozone absorption cross-sections – Part 2: Temperature dependence', *Atmospheric Measurement Techniques*, 7(2), pp. 625–636. doi: 10.5194/amt-7-625-2014.

Sitch, S. *et al.* (2007) 'Indirect radiative forcing of climate change through ozone effects on the land-carbon sink', *Nature*, 448(7155), pp. 791–794. doi: 10.1038/nature06059.

Spicer, C. W., Joseph, D. W. and Ollison, W. M. (2010) 'A Re-Examination of Ambient Air Ozone Monitor Interferences', *Journal* 405 *of the Air & Waste Management Association*, 60(11), pp. 1353–1364. doi: 10.3155/1047-3289.60.11.1353.

Turnipseed, A. A. *et al.* (2017) 'Use of a heated graphite scrubber as a means of reducing interferences in UV-absorbance measurements of atmospheric ozone', *Atmospheric Measurement Techniques*, 10(6), pp. 2253–2269. doi: 10.5194/amt-10-2253-2017.

Washenfelder, R. A. *et al.* (2008) 'Measurement of glyoxal using an incoherent broadband cavity enhanced absorption 410 spectrometer', *Atmospheric Chemistry and Physics*, 8(24), pp. 7779–7793. doi: 10.5194/acp-8-7779-2008.

Webb, E. K., Pearman, G. I. and Leuning, R. (1980) 'Correction of flux measurements for density effects due to heat and water vapour transfer', *Quarterly Journal of the Royal Meteorological Society*, 106(447), pp. 85–100. doi: 10.1002/qj.49710644707.

Wesely, M. L. (1989) 'Parameterization of surface resistances to gaseous dry deposition in regional-scale numerical models', *Atmospheric Environment (1967)*, 23(6), pp. 1293–1304. doi: 10.1016/0004-6981(89)90153-4.

415 Wesely, M. L. and Hicks, B. B. (2000) 'A review of the current status of knowledge on dry deposition', *Atmospheric Environment*, 34(12–14), pp. 2261–2282. doi: 10.1016/S1352-2310(99)00467-7.

Wolfe, G. M. *et al.* (2018) 'The NASA Carbon Airborne Flux Experiment (CARAFE): instrumentation and methodology', *Atmospheric Measurement Techniques*, 11(3), pp. 1757–1776. doi: 10.5194/amt-11-1757-2018.

Young, P. J. *et al.* (2018) 'Tropospheric Ozone Assessment Report: Assessment of global-scale model performance for global and 420 regional ozone distributions, variability, and trends', *Elementa*, 6(1), p. 10. doi: 10.1525/elementa.265.

Table 1: Summary of ROZE performance capabilities.

Specification	Value
Size	58 x 44 x 18 cm^3
Weight	19 kg
Power	< 200 W
Data rate	10 Hz
Precision (1σ, 1Hz)	6.7 x 10^8 molecules cm^{-3}
Accuracy	6.2%
Time response	50 ms
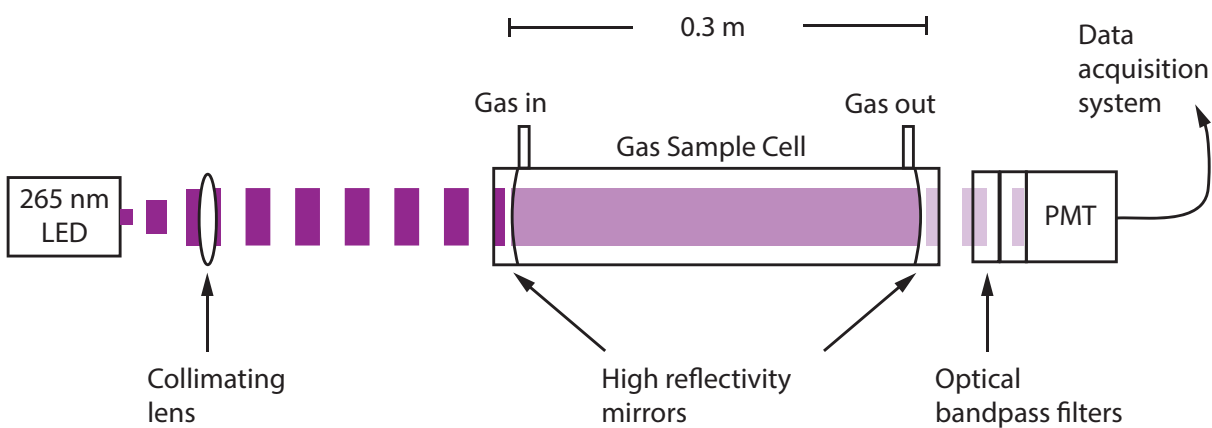
425 **Figure 1: Incoherent broadband cavity enhanced detection technique for O$_3$. A LED at 265 nm is collimated with a lens and coupled into the detection cell via high reflectivity mirrors (R > 99.7%) that comprise the optical cavity and create a long effective optical pathlength. The light attenuated by the sample is then detected using a photomultiplier tube (PMT) operated in analog mode. The sample enters and exits the cell orthogonal to the beam propagation.**

430
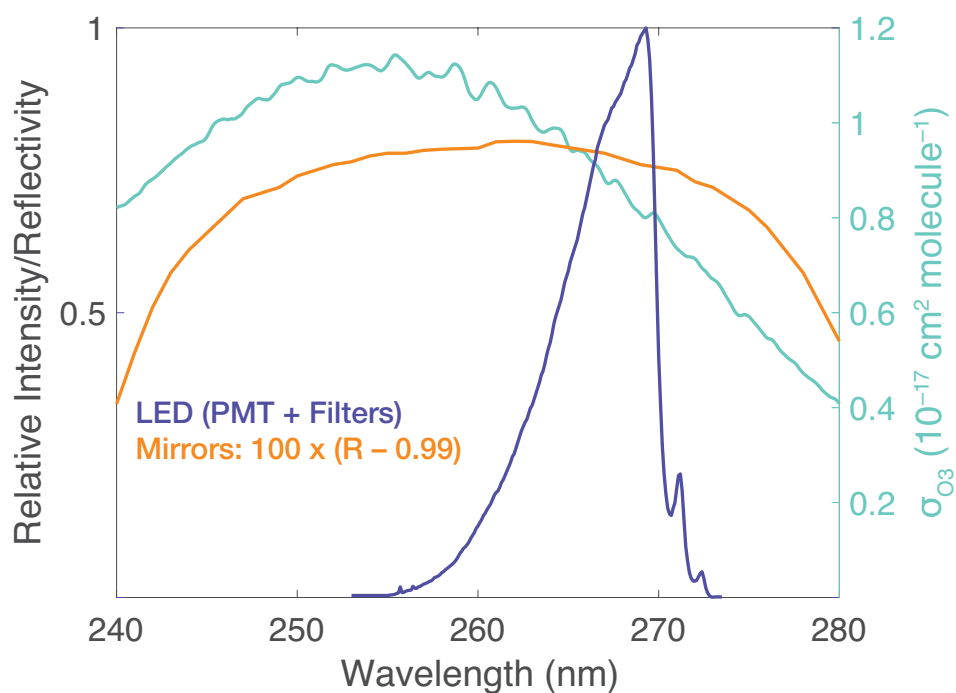
Figure 2: LED spectrum, mirror reflectivity, and O₃ absorption cross section: The LED (λ_{max} = 265 nm, FWHM = 10 nm) spectrum was measured using a grating spectrometer (0.1 nm resolution) with the instrument PMT and associated detector optics. The mirror curve depicts $100 \times [R - 0.99]$, where R is the reflectivity, over a range of wavelengths. The right axis shows the absorption cross section for the O₃ Hartley band. O₃ and Rayleigh cross sections were determined as the weighted average with the normalized intensity of the LED and PMT detector optics.

435
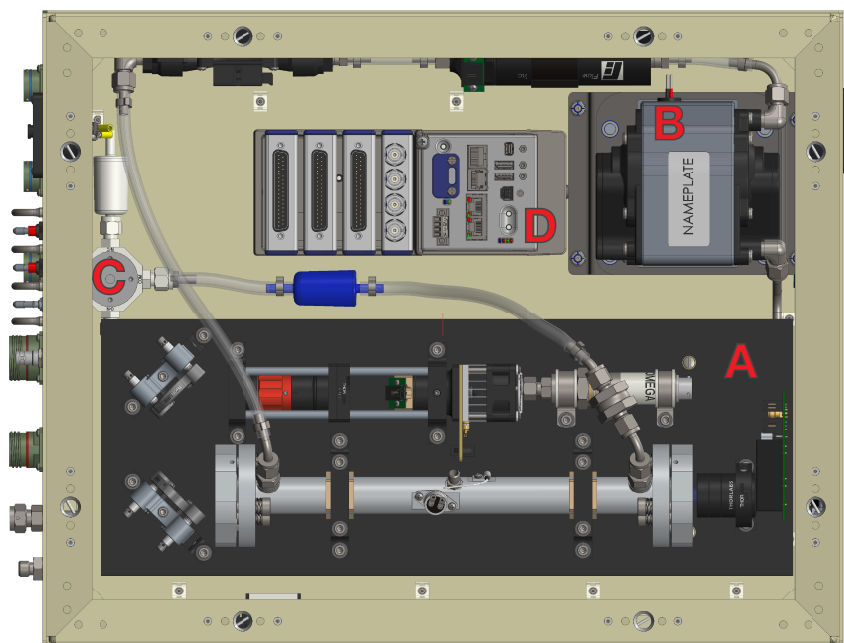
440

Figure 3: A top view of the ROZE instrument chassis. Major components include A) the optical plate, which consists of the LED assembly, associated optics, the optical cell, and PMT detector; B) The diaphragm pump which can pull up to ~18 SLM through the flow system; C) The 3-way valve which switches between the sample line and air scrubbed of O_3 using a Carulite filter; and D) The data acquisition system.

445
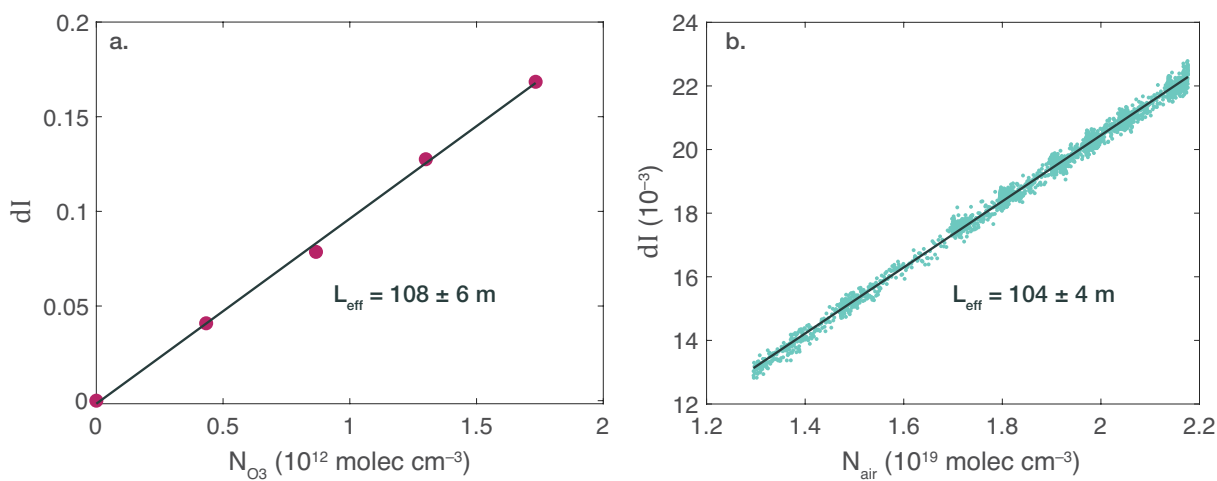
Figure 4: ROZE calibration: a) The effective pathlength (L_{eff}) as determined by attenuation (dI) due to known additions of O_3 from a commercial ozone-generator. The slope yields the effective pathlength as determined from Equation 1 in the text using the known O_3 absorption cross section; b) Attenuation due to Rayleigh scatter over a range of cell pressures. The slope of attenuation as a function of number density gives the pathlength using the known Rayleigh scattering cross section for zero air. The pathlength derived from both calibrations agree to within the 2σ fit uncertainty.
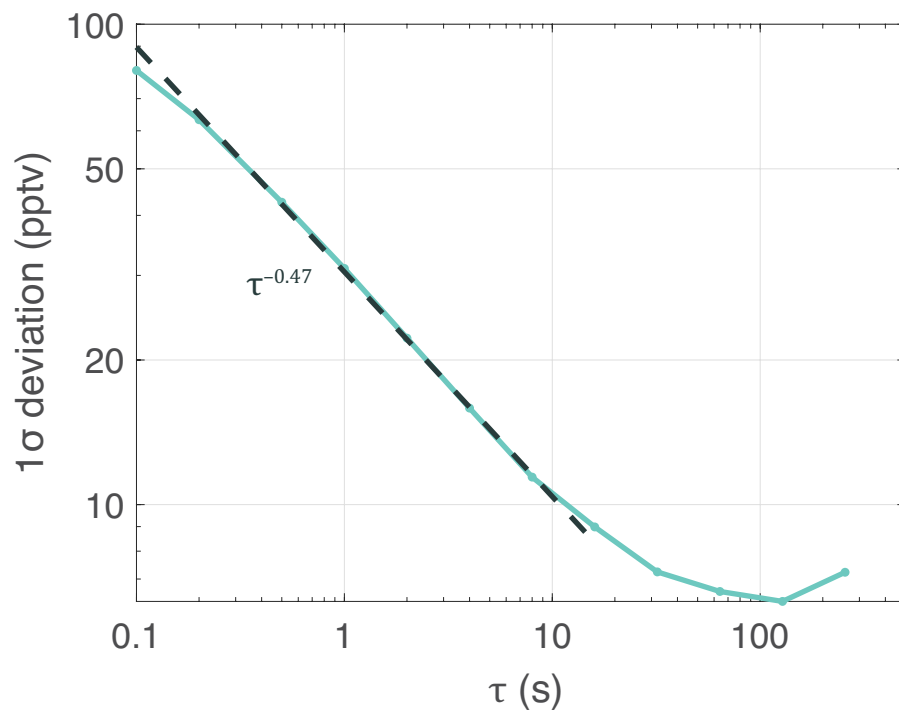
Figure 5: Allan deviation plot for 1.5 hr of sampling zero air at constant pressure (944 mbar). The 1σ precision is expressed in pptv equivalents of O_3 as a function of the integration time τ. The curve demonstrates a precision of 31 pptv in a 1 s integration time. The dashed line shows a $\tau^{-0.47}$ decay for short integration times (< 10 s), comparable to the $\tau^{-1/2}$ decay expected for white noise.

460
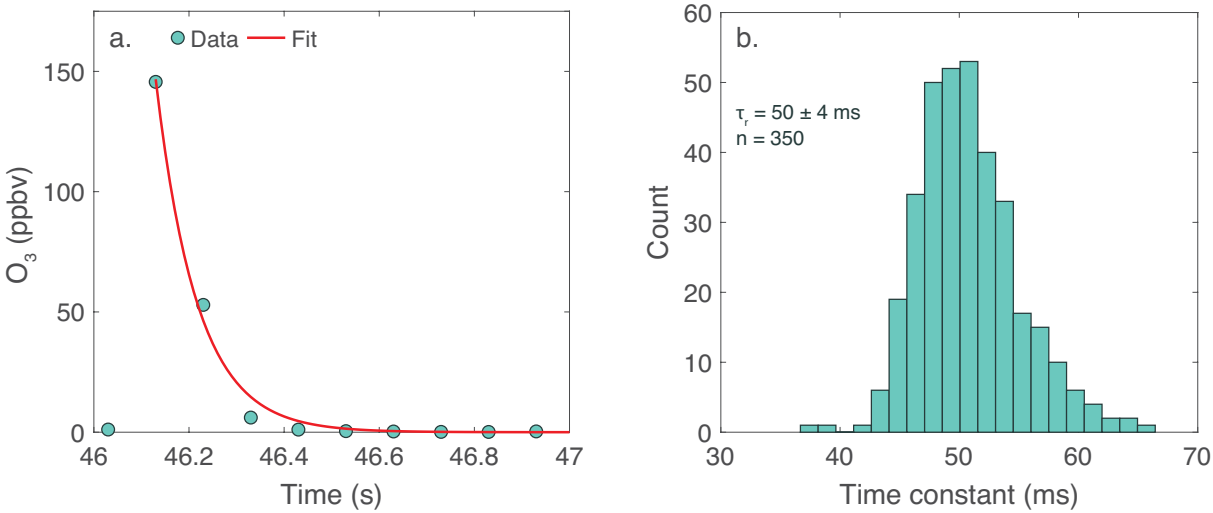
Figure 6: ROZE time response: a) Ozone was injected into the flow system via a pulsed valve at 2-second intervals with a sample flow of 18 SLM. An exponential decay function was fitted to each individual pulse (pulse data shown in blue; fit in red); b) Histogram of time constants for all 350 pulses. The *e*-folding decay time of 50 ± 4 ms corresponds to a 3*e*-fold cell flush rate of 9.5 Hz.

475
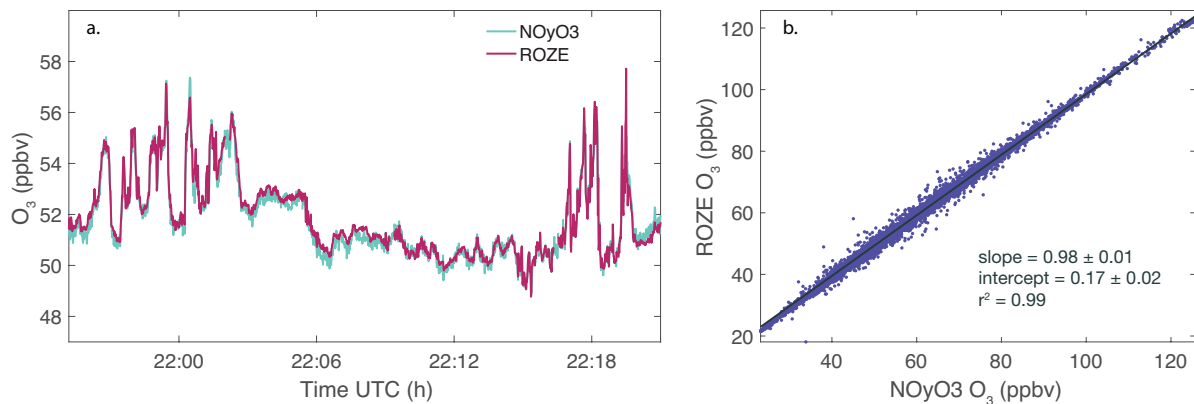
Figure 7: ROZE and NOyO3 measurements of O₃ from a FIREX-AQ flight on July 30, 2019 over the Northwestern US: a) Timeseries of ROZE and NOyO3 data (averaged to 1 s); b) Correlation plot of ROZE and NOyO3 O₃ measurements from the full flight. A linear fit to the data yields a slope of 0.98 ± .01 and an intercept of 0.17 ± 0.02 ppbv.

480
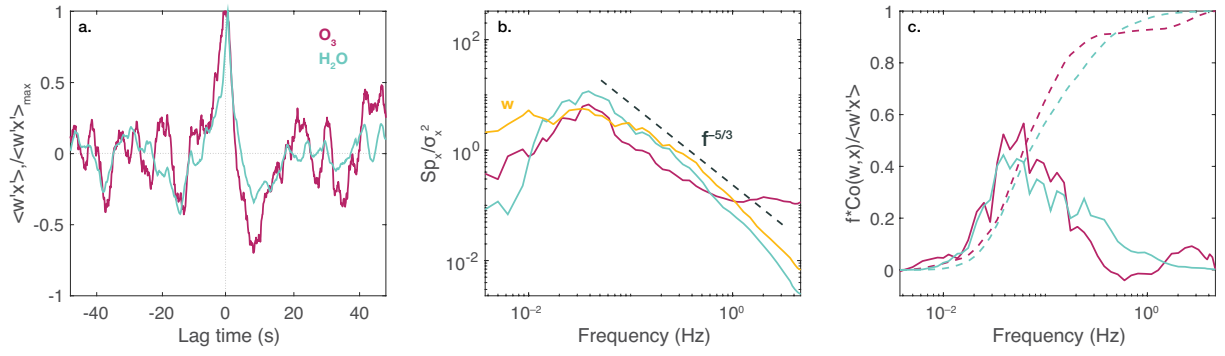
Figure 8: Example spectra from a 50 km flux leg at 170 m altitude during the July 17, 2019 flight over the Pacific Ocean:
a) Vertical wind-scalar (w and x respectively) cross covariance functions normalized by the maximum covariance for O_3
and water vapor; b) Power spectra normalized to total variance for w, O_3, and H_2O. The dashed line represents the $f^{-5/3}$
theoretical decay for the inertial subrange; c) Solid lines depict co-spectral power (frequency-multiplied and covariance-
normalized) of O_3 and H_2O with vertical wind. Dashed lines depict the respective ogives (cumulative integrals).

485

490